EINDHOVEN UNIVERSITY OF TECHNOLOGY

A monolithic numerical model to predict the EMI shielding performance of lossy dielectric polymer nanocomposite shields in a rectangular waveguide

Citation for published version (APA):
Van Loock, F., Anderson, P. D., & Cardinaels, R. (2024). A monolithic numerical model to predict the EMI shielding performance of lossy dielectric polymer nanocomposite shields in a rectangular waveguide: Design of an absorption-based sawtooth-shaped layer. *Applied Mathematical Modelling*, *134*, 108-125. https://doi.org/10.1016/j.apm.2024.05.029

Document license:
CC BY

DOI:
10.1016/j.apm.2024.05.029

Document status and date:
Published: 01/10/2024

Document Version:
Publisher's PDF, also known as Version of Record (includes final page, issue and volume numbers)

Please check the document version of this publication:

• A submitted manuscript is the version of the article upon submission and before peer-review. There can be important differences between the submitted version and the official published version of record. People interested in the research are advised to contact the author for the final version of the publication, or visit the DOI to the publisher's website.
• The final author version and the galley proof are versions of the publication after peer review.
• The final published version features the final layout of the paper including the volume, issue and page numbers.

Link to publication

General rights
Copyright and moral rights for the publications made accessible in the public portal are retained by the authors and/or other copyright owners and it is a condition of accessing publications that users recognise and abide by the legal requirements associated with these rights.

• Users may download and print one copy of any publication from the public portal for the purpose of private study or research.
• You may not further distribute the material or use it for any profit-making activity or commercial gain
• You may freely distribute the URL identifying the publication in the public portal.

If the publication is distributed under the terms of Article 25fa of the Dutch Copyright Act, indicated by the "Taverne" license above, please follow below link for the End User Agreement:

www.tue.nl/taverne

Take down policy
If you believe that this document breaches copyright please contact us at:

openaccess@tue.nl

providing details and we will investigate your claim.

Download date: 07. Jul. 2024

Applied Mathematical Modelling 134 (2024) 108–125

Contents lists available at ScienceDirect

Applied Mathematical Modelling

journal homepage: www.elsevier.com/locate/apm

A monolithic numerical model to predict the EMI shielding performance of lossy dielectric polymer nanocomposite shields in a rectangular waveguide: Design of an absorption-based sawtooth-shaped layer

F. Van Loock [a,*], P.D. Anderson [a], R. Cardinaels [a,b,*]

[a] Processing and Performance of Materials, Department of Mechanical Engineering, Eindhoven University of Technology, 5600MB Eindhoven, the Netherlands

[b] Soft Matter, Rheology and Technology, Department of Chemical Engineering, KU Leuven, 3001 Leuven, Belgium

ARTICLE INFO

Keywords:
Finite element model
EMI shielding
Waveguide
Polymer nanocomposite
Absorption-dominated shielding
Sawtooth layer

ABSTRACT

A three-dimensional numerical model is constructed to predict the EMI shielding performance of a polymer nanocomposite shield in a rectangular waveguide. The Helmholtz wave equation for the electric field is implemented in component form and the set of coupled equations is solved via the finite element approach. Mesh convergence and model verification is performed by comparing free space model predictions for a flat, uniform layer to benchmark solutions calculated via transfer matrix theory. The capability of the model is showcased by exploring the role of geometry on the shielding performance of a sawtooth-shaped composite layer in a rectangular waveguide. Increasing the inclusion angle of the sawtooth, which is proportional to the ratio of the sawtooth amplitude and repeat unit width, reduces the transmitted power through the shield and increases the ratio of absorption to reflection of wave power by the shield. Thus, a rational design of this sawtooth geometry allows to overcome the typical trade-off between total shielding effectiveness and wave absorption contribution, thereby resulting in highly performant absorption-dominated shields.

1. Introduction

Due to the increasing use of electronics and wireless technology in society, there is growing interest in the prevention of interference and cross-talk of electromagnetic (EM) waves [1]. Electromagnetic interference (EMI) can cause electronic components in critical applications such as medical devices and aerospace control and navigation systems to malfunction [2,3]. These components can be protected by a layer of shielding material where the incident wave power is reflected by the shield and/or absorbed throughout the shield [4]. Typical shielding materials are of metallic nature, these exhibit high values of shielding effectiveness within a large frequency range due to their high electrical conductivity [5]. Yet, metallic shields reflect most wave power to the environment. To avoid pollution by reflected EM waves, one can make use of polymer nanocomposite shielding materials, which are able to partially absorb the incident EM power via conductive and dielectric dissipation mechanisms [6–8]. These polymer-based shielding materials also offer improved mass-normalised mechanical properties, corrosion resistance and shape design flexibility with respect to metallic

* Corresponding authors.
E-mail addresses: F.Van.Loock@tue.nl (F. Van Loock), R.M.Cardinaels@tue.nl (R. Cardinaels).

https://doi.org/10.1016/j.apm.2024.05.029
Received 15 February 2024; Received in revised form 20 May 2024; Accepted 22 May 2024
Available online 29 May 2024
0307-904X/© 2024 The Author(s). Published by Elsevier Inc. This is an open access article under the CC BY license (http://creativecommons.org/licenses/by/4.0/).

materials. Typical polymer-based shielding materials are particulate composites comprising a conductive or non-conductive polymer matrix and conductive fillers (e.g. carbon nanotubes (CNTs)) [7,9]. The addition of filler material can also lead to enhanced mechanical and chemical stability [10–12]. There is substantial experimental evidence demonstrating that tailoring the nanocomposite layer design by, for instance, adding geometric features or by spatially controlling the electromagnetic properties can give improved shielding efficiency (i.e. absorption-dominated shielding) with respect to a flat and uniform nanocomposite shield [8,13–18]. One example in recent experimental literature are composite layers with 'zig-zag' or sawtooth shapes. Shen et al. produced multilayered thermoplastic polyurethane (TPU) - graphene films with a sawtooth geometry and measured the shielding performance of the sawtooth-shaped layers in the X-band frequency regime in a rectangular waveguide [14]. They reported that a sawtooth-shaped film may have a twofold higher shielding effectiveness than a flat film of identical thickness and electromagnetic properties. In addition, they demonstrated that shielding may transition from reflection-dominated for flat films to absorption-dominated for selected sawtooth geometries. A similar strategy was followed by He and co-workers, who introduced 'surface wrinkles' on a sandwich shield of copper and polydimethylsiloxane to enhance absorbance [19]. They attributed the reduced reflectance with increased wrinkle amplitude to an enlargement of the effective surface area interacting with the EM wave and interference of reflected EM waves between two interfaces of the wrinkle peaks. Research efforts on the design of absorption-based EMI shielding with polymer composites are, however, mostly dominated by time-consuming experimental trial-and-error design strategies [8,17,20–23].

Analytical models based on transmission line theory can be used to calculate the shielding performance of relatively simple layer designs (e.g. flat layers with a one-dimensional change of electromagnetic properties) [24–26]. These models often consider the specialised case of a planar wave in free space shielding conditions. However, the shielding response of a layer with more complex features such as 2D or 3D spatial variation of electromagnetic properties and/or geometry can, in many cases, not be calculated via closed-form analytical solutions [27,28]. In addition, shielding tests on polymer composite layers in the microwave frequency regime (i.e. in the frequency range from 0.3 to 300 GHz) are often conducted by making use of a rectangular waveguide in which the shield (and waves reflected and transmitted by the shield) are bounded by the waveguide walls. Accurate prediction of the shielding performance of a layer with complex geometric and/or property distribution features in a waveguide test requires the construction of a 3D numerical model [19,21,29,30].

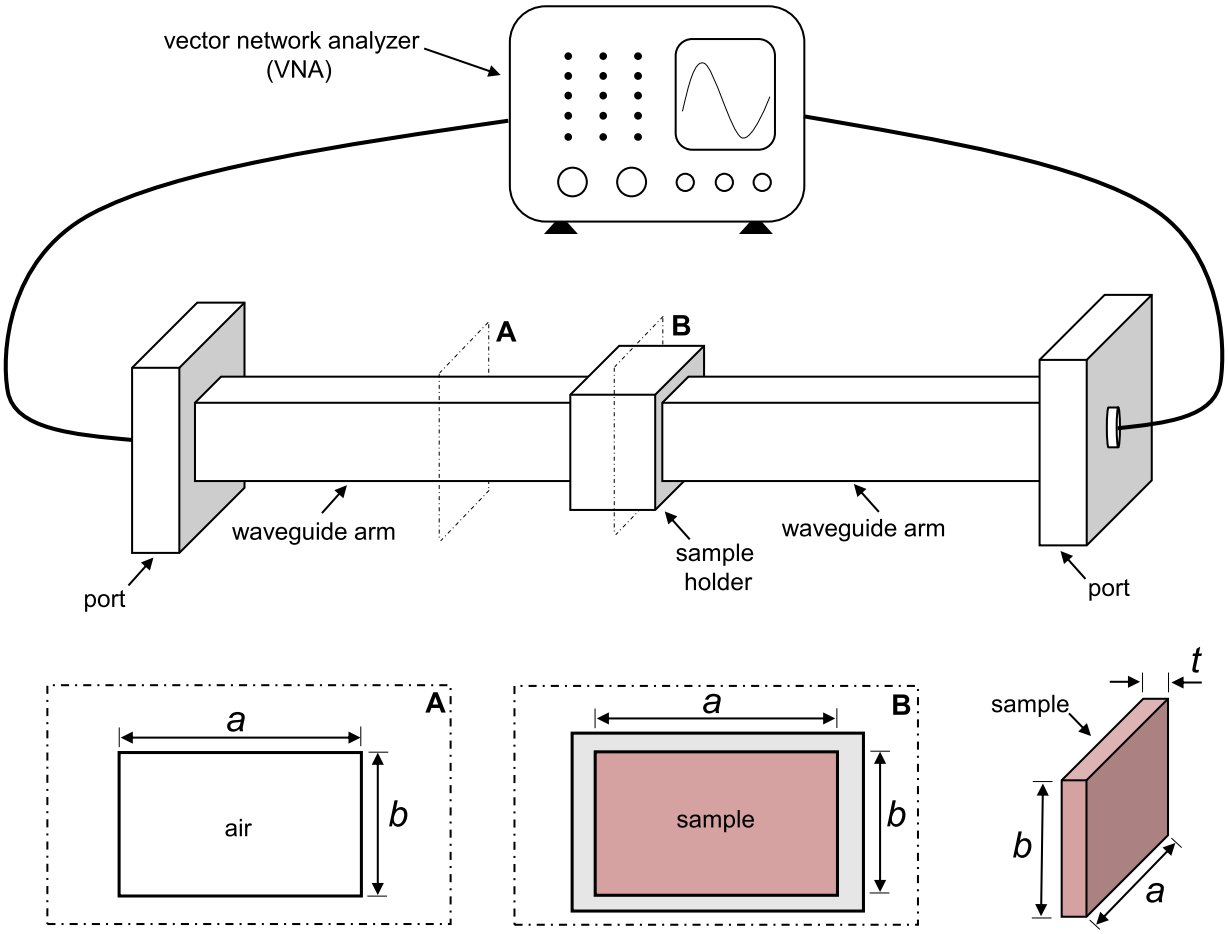

Fig. 1. Sketch of a rectangular waveguide test on a flat, layer-shaped shield.

The use of the finite element method (FEM) for numerical calculations of electromagnetic boundary value problems has been explored and developed in the 1970s to 1990s [31,32]. Due to its versatility and numerical efficiency, it has now become one of the standard numerical tools to simulate and analyse waveguide tests [28,33,34]. Although the original validation of finite element (FE) waveguide calculations focused on the prediction of the transmission and reflection response of lossy and/or anisotropic dielectric media of inorganic nature, the method is readily used to predict the shielding response of polymeric (nanocomposite) materials in waveguides. To illustrate, Karimi and co-workers made use of a FE model to predict the shielding response of a polycarbonate polymer layer with carbon fillers and used their experimentally validated model to explore the effect of layer thickness and frequency on the shielding response [35]. Recent studies conducted FE calculations to predict the shielding performance of more sophisticated composite shield designs including anisotropic properties [36], spatial variation in properties [21] and complex 3D topologies [29,37]. Most of these employ commercial finite element software packages, which are typically user-friendly but offer limited flexibility in spatial and temporal control of electromagnetic properties and insight and versatility in the use of numerical solving strategies for complex shield designs.

The scope of this paper is to present a numerical model to predict the shielding performance of polymer nanocomposite shields wherein the governing wave equation is solved in a direct, monolithic fashion. The monolithic approach allows the systems to have a wide range of material parameter gradients which is far more challenging in conventional decoupled methods. In addition, the approach is particularly suited for sophisticated, additively manufactured nanocomposite shields such as functionally graded layers with a combination of spatial variations in electromagnetic properties and complex 3D spatial architectures. The paper is structured as follows. First, the general boundary value problem for simulations of free space and waveguide shielding testing conditions is detailed and the matrix equations in component form are derived from the vector-based wave equation. Second, the finite element implementation is verified by making use of an analytical theory (free space) and a commercial FE package (waveguide) for a flat, uniform layer shield. Third, the capability of the model is demonstrated by computing the shielding performance of a sawtooth-shaped polymer composite layer in a rectangular waveguide and strategies are presented to manufacture absorption-dominated shields with high shielding effectiveness by tailoring the sawtooth geometry.

2. Model

2.1. Rectangular waveguide measurement setup

A simplified sketch of a typical shielding effectiveness measurement on a sample in a rectangular waveguide is shown in Fig. 1. A layer-shaped sample of dimensions $a \times b \times t$ is placed in a holder. The sample holder is connected to two hollow waveguide arms with a rectangular internal cross-section with width a and height b. Dimensions a and b dictate the test frequency regime in which only one transverse electric wave mode (TE_{01}) can propagate [25]. The waveguide is connected to a vector network analyzer (VNA) via a pair of coaxial cables. The VNA generates a wave signal at a selected frequency f_0 and measures the power reflected by the sample and that transmitted through the sample.

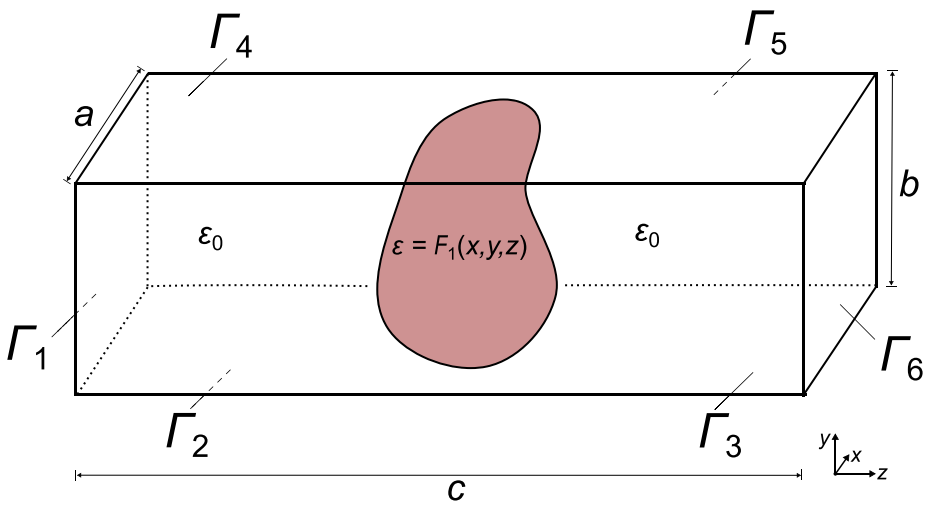

Fig. 2. Sketch of the boundary value problem of an arbitrarily shaped polymer composite sample placed in a rectangular waveguide. The value of the complex permittivity within the sample can be an arbitrary function of the spatial coordinates.

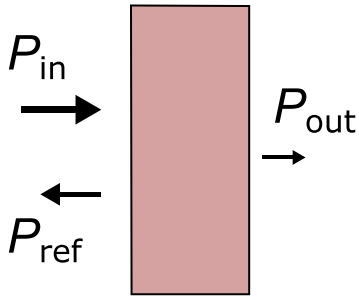

Fig. 3. Definition of power values for a shield subjected to a single incident wave (on the left side).

2.2. Boundary value problem

A three-dimensional model is constructed to compute the electric field $\boldsymbol{E}$ distribution within and around a lossy dielectric material sample of arbitrary shape placed in a rectangular waveguide. The corresponding boundary value problem is illustrated in Fig. 2. The material of the sample is endowed with a complex-valued relative permittivity ε which may be a function of spatial coordinates x, y and z (the value of the relative permittivity in the free space of the waveguide, ε_0, is equal to 1). In this work, we assume that the sample material is non-magnetic. The governing Maxwell equations can be simplified to the Helmholtz vector wave equation [28]:

$$\nabla \times (\nabla \times \boldsymbol{E}) - k_0^2 \varepsilon \boldsymbol{E} = \boldsymbol{0} \tag{1}$$

where k_0 ($= 2\pi f_0/c_0$) is the free space wavenumber and c_0 (≈ 2.998 m s^{-1}) the speed of light. Assuming that the waveguide operates at k_0 values where only the dominant TE_{01} wave mode can propagate, the following boundary conditions are used for $\boldsymbol{E}$ on the inlet Γ_1 (with $f(x) = \sin(\pi x/a)$, where a is the longest of the two dimensions of the waveguide cross-section, see Fig. 1) and outlet Γ_6 (with $f(x) = 0$) of the waveguide [28,38]:

$$\boldsymbol{n} \times (\nabla \times \boldsymbol{E}) + ik_z \boldsymbol{n} \times (\boldsymbol{n} \times \boldsymbol{E}) = -2E_0 ik_z f(x) \exp(-ik_z z)\mathbf{e_y} \tag{2}$$

where $\boldsymbol{n}$ is the unit normal vector on the boundary plane, E_0 a field amplitude (equal to 1 for all calculations presented in this study) and k_z the TE_{01} wavenumber:

$$k_z = \sqrt{k_0^2 - \left(\frac{\pi}{a}\right)^2}. \tag{3}$$

On the walls of the waveguide (Γ_2 to Γ_5) we assume perfect electric conductance (PEC):

$$\boldsymbol{n} \times \boldsymbol{E} = \boldsymbol{0}. \tag{4}$$

The waveguide model can be extended to the important case of an infinitesimally large shield with a one-dimensional property gradient subjected to an orthogonally-incident transverse electromagnetic (TEM) wave in free space [39,40]. Here, the values of ε are assumed to be independent of the y- and z-coordinates but may depend on the x-coordinate. To predict the shielding performance of such a layer in free space, i.e. without the presence of the waveguide walls, we assume $k_z = k_0$ and modify the boundary conditions as follows. First, we chose $f(x) = 1$ in Eq. (2) for Γ_1 . Second, we replace Eq. (4) on the waveguide walls (Γ_2 to Γ_5) with a pair of periodic boundary conditions:

$$\begin{cases} \boldsymbol{E}_{\Gamma_3} = \boldsymbol{E}_{\Gamma_5} \\ \boldsymbol{E}_{\Gamma_2} = \boldsymbol{E}_{\Gamma_4} \end{cases}. \tag{5}$$

2.3. Numerical method

The electric field $\boldsymbol{E}$ is computed by solving Eq. (1) with boundary conditions defined via Eqs. (2) and (4) (PEC conditions) or (5) (free space conditions). We make use of a monolithic calculation approach whereby the set of coupled, real-valued equations derived from Eqs. (1) to (5) are simultaneously solved. To this end, we write and implement the wave equation, Eq. (1), via the following real-valued component form:

$$\begin{bmatrix} -\left(\frac{\partial^2}{\partial y^2}+\frac{\partial^2}{\partial z^2}\right)-k_0^2\varepsilon' & -k_0^2\varepsilon'' & \frac{\partial^2}{\partial x\partial y} & 0 & \frac{\partial^2}{\partial x\partial z} & 0 \\ k_0^2\varepsilon'' & -\left(\frac{\partial^2}{\partial y^2}+\frac{\partial^2}{\partial z^2}\right)-k_0^2\varepsilon' & 0 & \frac{\partial^2}{\partial x\partial y} & 0 & \frac{\partial^2}{\partial x\partial z} \\ \frac{\partial^2}{\partial x\partial y} & 0 & -\left(\frac{\partial^2}{\partial x^2}+\frac{\partial^2}{\partial z^2}\right)-k_0^2\varepsilon' & -k_0^2\varepsilon'' & \frac{\partial^2}{\partial y\partial z} & 0 \\ 0 & \frac{\partial^2}{\partial x\partial y} & k_0^2\varepsilon'' & -\left(\frac{\partial^2}{\partial x^2}+\frac{\partial^2}{\partial z^2}\right)-k_0^2\varepsilon' & 0 & \frac{\partial^2}{\partial y\partial z} \\ \frac{\partial^2}{\partial x\partial z} & 0 & \frac{\partial^2}{\partial y\partial z} & 0 & -\left(\frac{\partial^2}{\partial x^2}+\frac{\partial^2}{\partial y^2}\right)-k_0^2\varepsilon' & -k_0^2\varepsilon'' \\ 0 & \frac{\partial^2}{\partial x\partial z} & 0 & \frac{\partial^2}{\partial y\partial z} & k_0^2\varepsilon'' & -\left(\frac{\partial^2}{\partial x^2}+\frac{\partial^2}{\partial y^2}\right)-k_0^2\varepsilon' \end{bmatrix} \begin{bmatrix} E_x' \\ E_x'' \\ E_y' \\ E_y'' \\ E_z' \\ E_z'' \end{bmatrix} = \mathbf{0}, \tag{6}$$

where we have used the following definition for the 6 electric field components:

$$\begin{pmatrix} E_x \\ E_y \\ E_z \end{pmatrix} = \begin{pmatrix} E_x' + E_x''i \\ E_y' + E_y''i \\ E_z' + E_z''i \end{pmatrix}. \tag{7}$$

Likewise, we rewrite and implement the boundary conditions given by Eq. (2) in component form. Assuming the unit normal vector $\boldsymbol{n}$ to equal (0, 0, −1) at the inlet, the condition at the inlet reads:

$$\begin{pmatrix} \frac{\partial}{\partial z} & k_z & 0 & 0 & -\frac{\partial}{\partial x} & 0 \\ -k_z & \frac{\partial}{\partial z} & 0 & 0 & 0 & -\frac{\partial}{\partial x} \\ 0 & 0 & \frac{\partial}{\partial z} & k_z & -\frac{\partial}{\partial y} & 0 \\ 0 & 0 & -k_z & \frac{\partial}{\partial z} & 0 & -\frac{\partial}{\partial y} \end{pmatrix} \begin{pmatrix} E_x' \\ E_x'' \\ E_y' \\ E_y'' \\ E_z' \\ E_z'' \end{pmatrix} = \begin{pmatrix} 0 \\ 0 \\ 0 \\ -2E_0 k_z f(x) \end{pmatrix}. \tag{8}$$

At the outlet of the waveguide, $\boldsymbol{n} = (0, 0, 1)$, and the condition reads:

$$\begin{pmatrix} -\frac{\partial}{\partial z} & k_z & 0 & 0 & \frac{\partial}{\partial x} & 0 \\ -k_z & -\frac{\partial}{\partial z} & 0 & 0 & 0 & \frac{\partial}{\partial x} \\ 0 & 0 & -\frac{\partial}{\partial z} & k_z & \frac{\partial}{\partial y} & 0 \\ 0 & 0 & -k_z & -\frac{\partial}{\partial z} & 0 & \frac{\partial}{\partial y} \end{pmatrix} \begin{pmatrix} E_x' \\ E_x'' \\ E_y' \\ E_y'' \\ E_z' \\ E_z'' \end{pmatrix} = \begin{pmatrix} 0 \\ 0 \\ 0 \\ 0 \end{pmatrix}. \tag{9}$$

We have implemented Eqs. (6) to (9) via an in-house build FE code originally developed to solve complex fluid mechanics problems, but particularly suited to deal with multiple components that have a wide range of material properties. The code has been extensively verified and validated in earlier work, see, for example, the work of Anderson and co-workers [41–46]. Since existing building blocks in the modular code are combined in this work, no separate verification is added here. The set of coupled equations, Eqs. (6) to (9), are discretised making use of the GMSH software [47] with 10-node quadratic tetrahedral elements. After the weak finite element formulation is obtained, the resulting set of matrix equations is directly solved via the PARDISO package with the unsymmetric, real matrix solver setting compatible with the FE code [48]. Note that the element size was refined close to and within the sample domain. Free space calculations with periodic boundary conditions were conducted with periodic meshes on the pairs of corresponding boundary surfaces (i.e. Γ_3 - Γ_5 and Γ_2 - Γ_4) via the periodic surface option in GMSH.

2.4. Shielding performance definitions and their calculation from the predicted electric field

Consider a polymer composite shield with an incident wave of power P_{in}, see Fig. 3. Part of the incident wave power, P_{ref}, is reflected by the shield. The power absorbed by the shield, P_{abs}, reads:

$$P_{\text{abs}} = P_{\text{ent}} - P_{\text{out}}, \tag{10}$$

where P_{ent} is the proportion of the incident wave power that is not reflected and 'enters' the shield and P_{out} is the wave power that is transmitted through the shield. Shielding performance figures are the reflectance R:

$$R = \frac{P_{\text{ref}}}{P_{\text{in}}}, \tag{11}$$

the transmittance T:

$$T = \frac{P_{\text{out}}}{P_{\text{in}}}, \tag{12}$$

and absorbance A:

$$A = \frac{P_{\text{abs}}}{P_{\text{in}}}. \tag{13}$$

Balance of energy gives:

$$A = 1 - R - T. \tag{14}$$

The total shielding effectiveness, SE_{tot}, is a figure often used to rank the performance of different shields:

$$SE_{\text{tot}} = -10\log_{10}(T). \tag{15}$$

The values of A, R, and T are calculated based on the predicted electric field distributions at the waveguide's in- and outlet. The value of R is computed by integration of the electric field at the inlet Γ_1 [28]:

$$R = \left| \frac{2\exp(-ik_z z_1)}{E_0 ab} \iint_{S=\Gamma_1} \boldsymbol{E}(x,y,z_1)\cdot f(x)\mathbf{e}_y \mathrm{d}S - \exp(-2ik_z z_1) \right|^2, \tag{16}$$

where $f(x) = \sin(\pi x/a)$ for waveguide testing conditions and $f(x) = 1$ for free space conditions. In our implementation, $z_1 = 0$. The transmittance T is calculated by integrating the electric field at the outlet Γ_6 [28]:

$$T = \left| \frac{2\exp(ik_z z_2)}{E_0 ab} \iint_{S=\Gamma_6} \mathbf{E}(x,y,z_2)\cdot f(x)\mathbf{e}_y \mathrm{d}S \right|^2, \tag{17}$$

where $z_2 = c$. The value of the absorbance, A, is calculated via Eq. (14).

3. Verification of the model for a flat, uniform layer

Extensive mesh convergence and model verification studies were conducted by comparing numerical predictions (with free space boundary conditions) to analytical solutions for the shielding performance of a flat, uniform layer in the X-band regime (8 GHz $< f_0 <$ 12 GHz). We have selected the dimensions of the simulation domain ($a = 22.86$ mm, $b = 10.16$ mm, $c = 220$ mm) to correspond to a WR90 waveguide which is used in practice to measure shielding data in the X-band regime. Different combinations of values for the permittivity and layer thickness were considered. Recall that the mesh size is refined close to and within the layer. Mesh size was controlled by choosing the element size l_e within the layer material and at the waveguide's inlet and outlet to be equal to a fraction of the corresponding medium's wavelength:

$$l_e = \frac{\lambda_i}{s}, \tag{18}$$

where $\lambda_i = \lambda_0 = c_0/f_0$ is the wavelength at the waveguide's inlet and outlet and $\lambda_i = \mathrm{Re}\left(\lambda_0 / \sqrt{\varepsilon}\right)$ is the transmission line guide wavelength [49]. The transition of element size in the waveguide arm from layer surface to inlet or outlet in the waveguide arm is controlled via the default GMSH size constraint options.

A typical mesh convergence and verification result is shown in Fig. 4a. Numerical predictions for the shielding performance figures (R, T, A) for a layer of thickness $t = 1$ mm and $\varepsilon = 30 - 10i$ are plotted as a function of s for $f_0 = 10$ GHz. The selected reference value of ε is representative for a polymer nanocomposite material with an intermediate nanofiller loading (i.e. before percolation) [6]. Benchmark analytical solutions for R, T and A calculated via transfer matrix theory (see Appendix A) are also included. Numerical and analytical predictions are in excellent agreement for a sufficiently large value of s (> 5, corresponding to a total number of elements in the simulation domain close to 50 000). Insight into mesh convergence behaviour is obtained by plotting the relative error between the analytical and numerical solution as a function of s. This is shown in Fig. 4b, where the error for T is plotted as a function of s for four different test cases, including different combinations of sample thickness and relative permittivity. The slope of the error versus s data for the different cases is similar, the relative error is below 1% when s exceeds 5 for all explored test cases in this study. The relative error in R and T is now plotted as a function of the number of nodes in the simulation domain, n_{nod}, for the selected case studies, see Figs. 4c and d. The data indicate a convergence rate with a slope close to 2. The predicted contour plots of the normalised electric field magnitude in the y-direction, $P_y = \sqrt{\left(E_y^{'}\right)^2 + \left(E_y^{''}\right)^2}/E_0$, are shown in Fig. 5 for a selected case ($t = 5$ mm and $\varepsilon = 30 - 10i$) for a low and high value of s. These plots illustrate the progressive increase of smoothness of the predicted fields when transitioning from a coarse ($s = 2$) to a more refined ($s = 10$) mesh for which the shielding performance predictions have sufficiently converged.

An additional verification study was conducted by comparing model predictions for a flat, uniform layer in an X-band waveguide measurement condition (PEC boundary conditions) with those provided by a commercially available FE software package (Ansys HFSS module, 2023). Various combinations of the values for the permittivity and layer thickness were investigated and good agreement between the predictions of both models was found for the entire X-band frequency regime. This is illustrated in Figs. 6a and b, where model predictions for R, T and A for two selected case studies are compared. We also note that the relative difference between total shielding effectiveness values predicted by the model (for $s > 5$) and those predicted by the Ansys model was found to be lower than 2.5% within the X-band frequency range for the selected values of permittivity and layer thickness in the verification study.

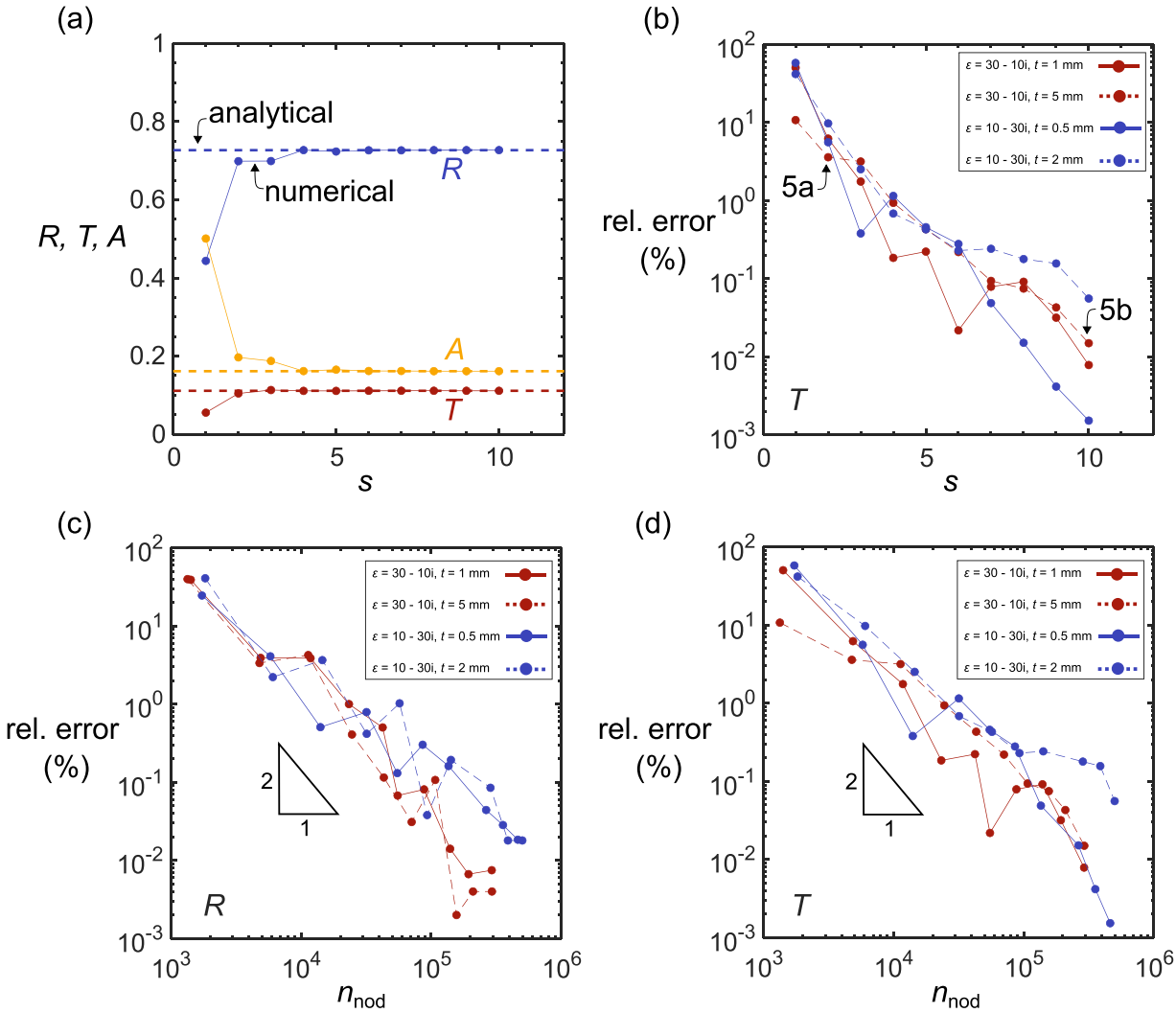

Fig. 4. (a) Numerical predictions with free space boundary conditions for R, T, and A for a uniform layer with $t = 1$ mm and $\varepsilon = 30 - 10i$ as function of s for $f_0 = 10$ GHz. Analytical benchmark predictions via the transfer matrix model detailed in Appendix A are also included. (b) Relative error between numerical and analytical predictions for T as a function of s for 4 test cases ($f_0 = 10$ GHz). Predicted contour plots of the normalised electric field for two selected cases are shown in Fig. 5. (c) Relative error between numerical and analytical predictions for R as a function of the number of nodes, n_{nod}, for 4 test cases ($f_0 = 10$ GHz). (d) Relative error between numerical and analytical predictions for T as a function of the number of nodes, n_{nod}, for 4 test cases ($f_0 = 10$ GHz).

4. Numerical case study: sawtooth-shaped polymer nanocomposite shield

The numerical model can be used to elucidate the role of complex geometrical features of polymer nanocomposite shields on their EMI shielding performance. Recall the sawtooth-shaped polymer composite shield explored by Shen and co-workers [14]. Depending on the sawtooth-geometry they demonstrated that shielding may transition from reflection-based ($A/R < 1$) for flat films to absorption-based ($A/R > 1$) while maintaining sufficiently high shielding effectiveness. In this section, we illustrate the potential of the numerical model to analyse the role of sawtooth geometry on the shielding performance of the polymer nanocomposite layer and illustrate how the model can be used as an alternative to more common experimental trial-and-error methods to reveal optimal geometries. We will focus on the effects of geometry and permittivity on the total shielding effectiveness SE_{tot} and the dominant shielding mechanism (i.e. absorption or reflection-dominated shielding) via the value of the ratio A/R. Consider a sawtooth-shaped shield with thickness t placed in a rectangular X-band waveguide of width a (= 22.86 mm), height b (= 10.16 mm) and length c (= 220 mm). A two-dimensional sketch of such a shield comprising of two base units in the x-z plane is shown in Fig. 7. We assume the geometry of the layer to be independent of the out of plane y-coordinate. Different sawtooth-shaped layer designs can be realised by changing the amplitude d and width w of a periodic base unit. In general, the shielding performance of the sawtooth-shaped layer in the rectangular waveguide is dependent upon the following list of variables:

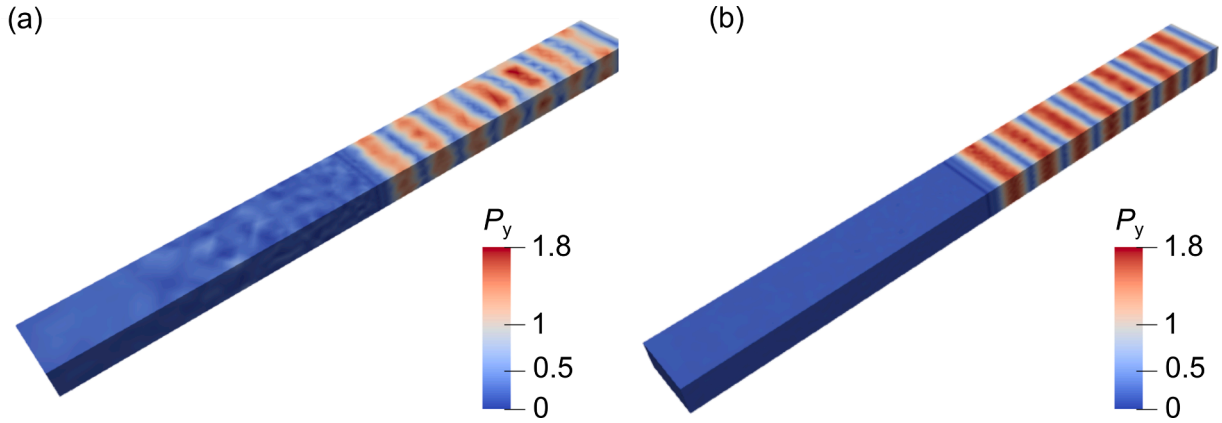

Fig. 5. Predicted contours of the normalised electric field magnitude, P_y, for the case $t = 5$ mm and $\varepsilon = 30 - 10i$ for two selected mesh size cases ($s = 2$ and $s = 10$, see Eq. (18)), see Fig. 4.

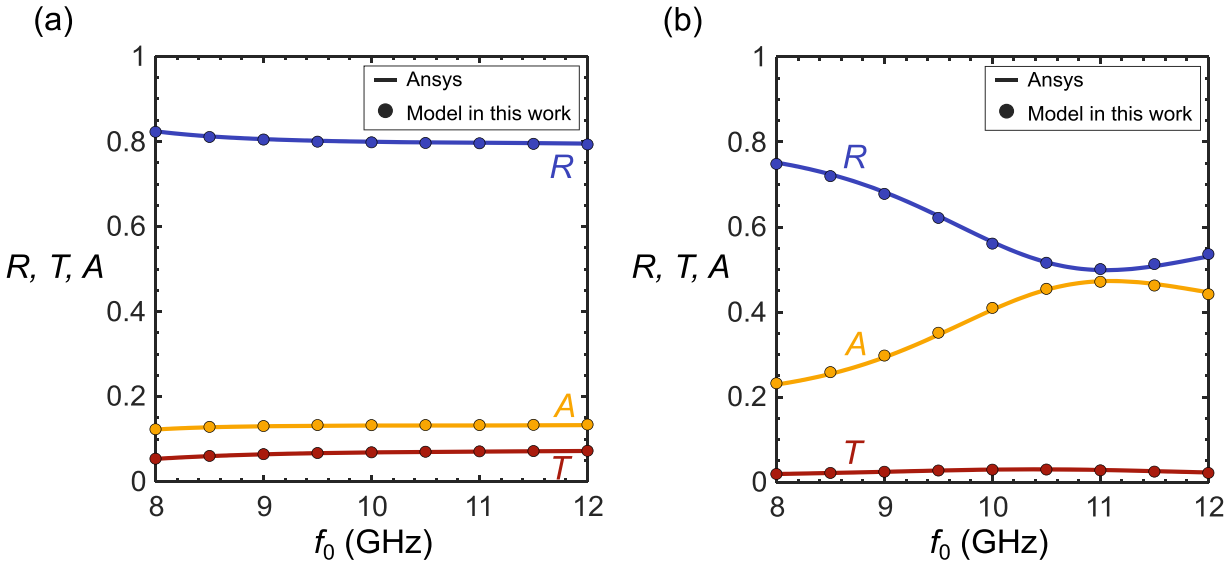

Fig. 6. Predicted values for R, T, and A as a function of frequency, f_0, for a rectangular waveguide measurement on a flat, uniform layer with $\varepsilon = 30 - 10i$ in the X-band frequency regime by the FE model developed in this work: (a) $t = 1$ mm and (b) $t = 5$ mm. Predicted values by a commercial FE model (Ansys) are included.

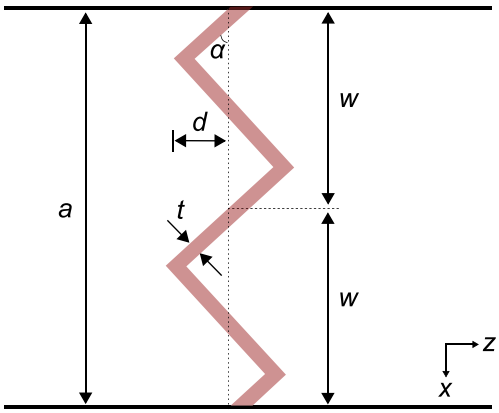

Fig. 7. Two-dimensional sketch of a sawtooth-shaped layer of thickness t comprising of two periodic base units with inclusion angle $\alpha = \tan^{-1}(4d/w)$. The layer is placed in a rectangular waveguide of width a.

$$\{w, d, t, a, b, c, \lambda_0, \varepsilon\}. \tag{19}$$

In this case study, we will focus on the role of geometry and the value of the permittivity of a sawtooth-shaped layer on the shielding performance. The waveguide dimensions (*a, b, c*) of the X-band waveguide are constant in this study. A list of physically relevant, non-dimensional parameters reads:

$$\left\{\alpha, \frac{a}{w}, \frac{t}{\lambda_0}, \varepsilon\right\}, \tag{20}$$

where the inclusion angle $\alpha = \tan^{-1}(4d/w)$ is a measure for the alignment of an individual sawtooth strut with respect to the nominal wave propagation direction (along the *z*-axis). Note that $\alpha = 0^\circ$ corresponds to a flat layer. The non-dimensional parameter a/w is an integer and corresponds to the number of repeated base units used to construct the sawtooth layer. The ratio t/λ_0 compares the layer thickness to the nominal wavelength.

A parametric study is conducted with the finite element model by making use of 4 mesh prototypes (a/w = 1, 2, 4, 16). An illustration of a meshed domain for $a/w = 1$ and $a/w = 4$ for identical values of α (= 20°) is included in Fig 8. The number of elements is a function of the geometry and lies in the range of 50 000 to 150 000. An illustration of the typical convergence behavior of the numerical predictions for selected cases explored in the parametric study is included in the supplementary information. First, the effect of inclusion angle α is analyzed for a selected reference value of layer thickness t (= 2 mm) and wavelength λ_0 ($= c_0/f_0 = 30$ mm, i.e. f_0 = 10 GHz). The selected reference value of the relative permittivity ($\varepsilon = 45 - 60i$) is assumed to be independent of frequency and falls in the X-band permittivity regime of a CNT-polymer nanocomposite with a relatively low filler content [6,50]. The calculated value of SE_{tot} is plotted in Fig. 9a as a function of α for a/w ranging from 1 to 16. For low to moderate values of α (i.e. in the range of 0° to 50°) the value of SE_{tot} mildly increases with increasing value of α and the SE_{tot} versus α trend is close to independent of the value of a/w. For larger angles, the α-SE_{tot} data show an increased sensitivity to the number of base units per waveguide width. The decrease in transmitted wave power with increasing inclusion angle value (for a selected value of a/w) can also be observed on contour plots of the predicted normalised electric field magnitude, P_y, see Fig. 10. The observation of an increase in shielding effectiveness with increase in inclusion angle at identical values of a/w and for identical material properties agrees with the experimental findings of Shen et al. [14].

The A/R versus α data plotted in Fig 9b demonstrate a similar trend: the absorbance increases with increasing value of α, and there is a significant effect of a/w for values of α exceeding 50°. The observed increase of both SE_{tot} and A/R with increasing value of the inclusion angle is caused by the increased obliqueness between the nominal wave propagation direction and the sawtooth strut. The

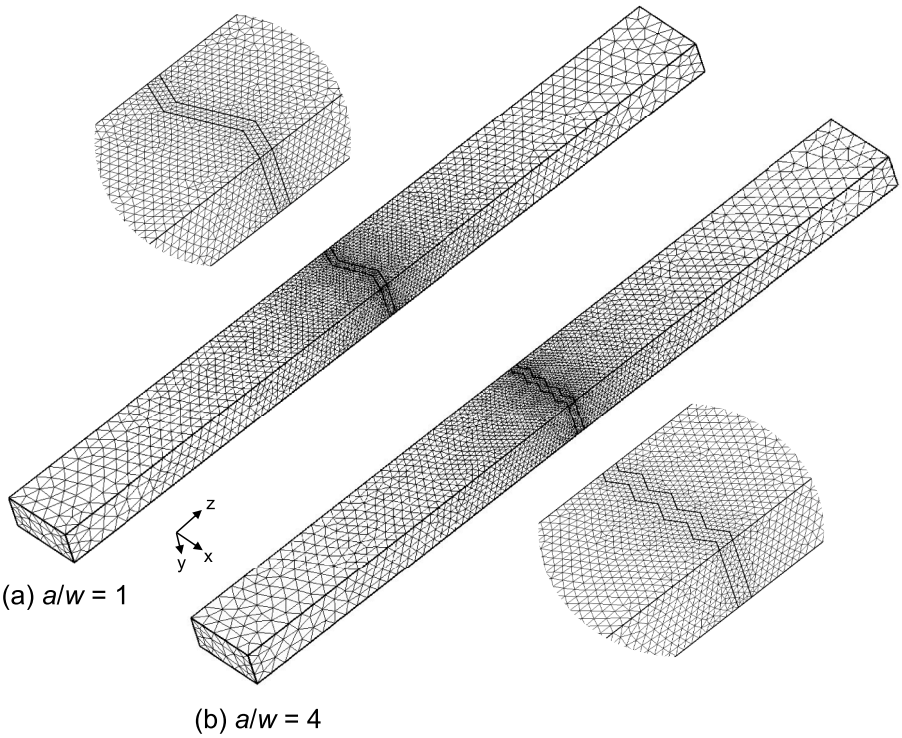

Fig. 8. Illustration of meshed WR90 waveguide domains comprising a sawtooth-shaped shield of thickness t equal to 2 mm made of one base unit ($a/w = 1$) and (b) 4 base units ($a/w = 4$). The inclusion angle α (= 20°) is identical for the shields in (a) and (b). Inserts are magnifications of the sawtooth layers.

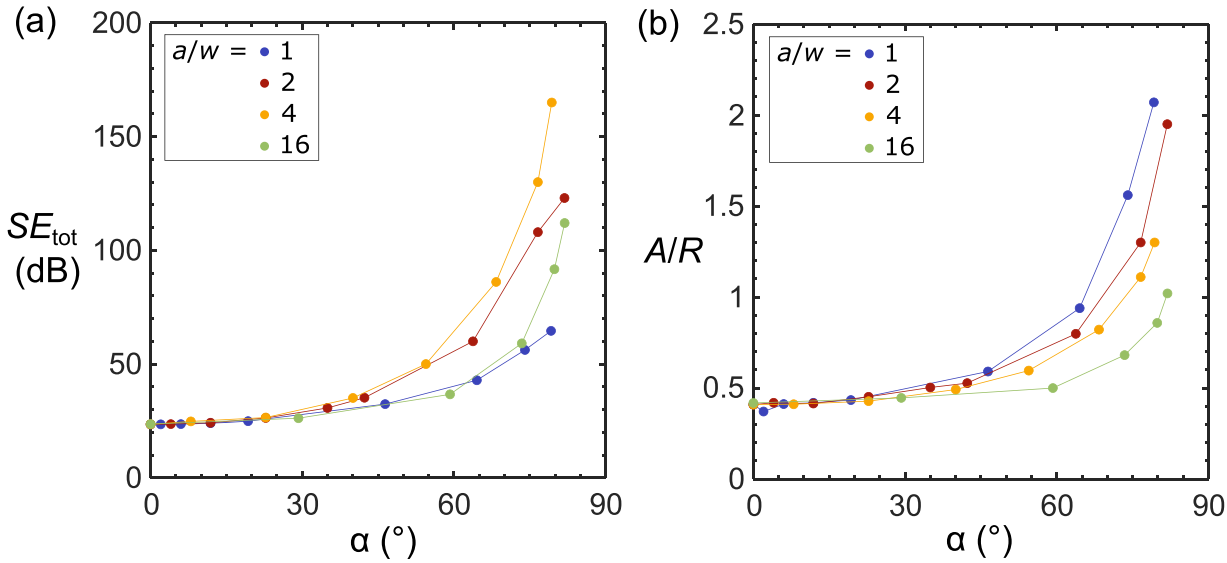

Fig. 9. (a) Total shielding effectiveness SE_{tot} and (b) A/R ratio as a function of inclusion angle α for sawtooth-shaped layers with a/w ranging from 1 to 16. Calculations were conducted for $t = 2$ mm, $\lambda_0 = 30$ mm, and $\varepsilon = 45 - 60i$.

decrease in transmitted power and increase in the ratio of absorbed to reflected power with increasing value of the inclusion angle is governed by different, possibly competing mechanisms. First, the oblique incidence of the wave onto the sawtooth strut leads to reflection of waves in the space between the peaks of the shield which are not aligned with the incident wave direction. The local reflectance of the individual struts is depending on the inclusion angle: it may either decrease or increase with increasing value of α

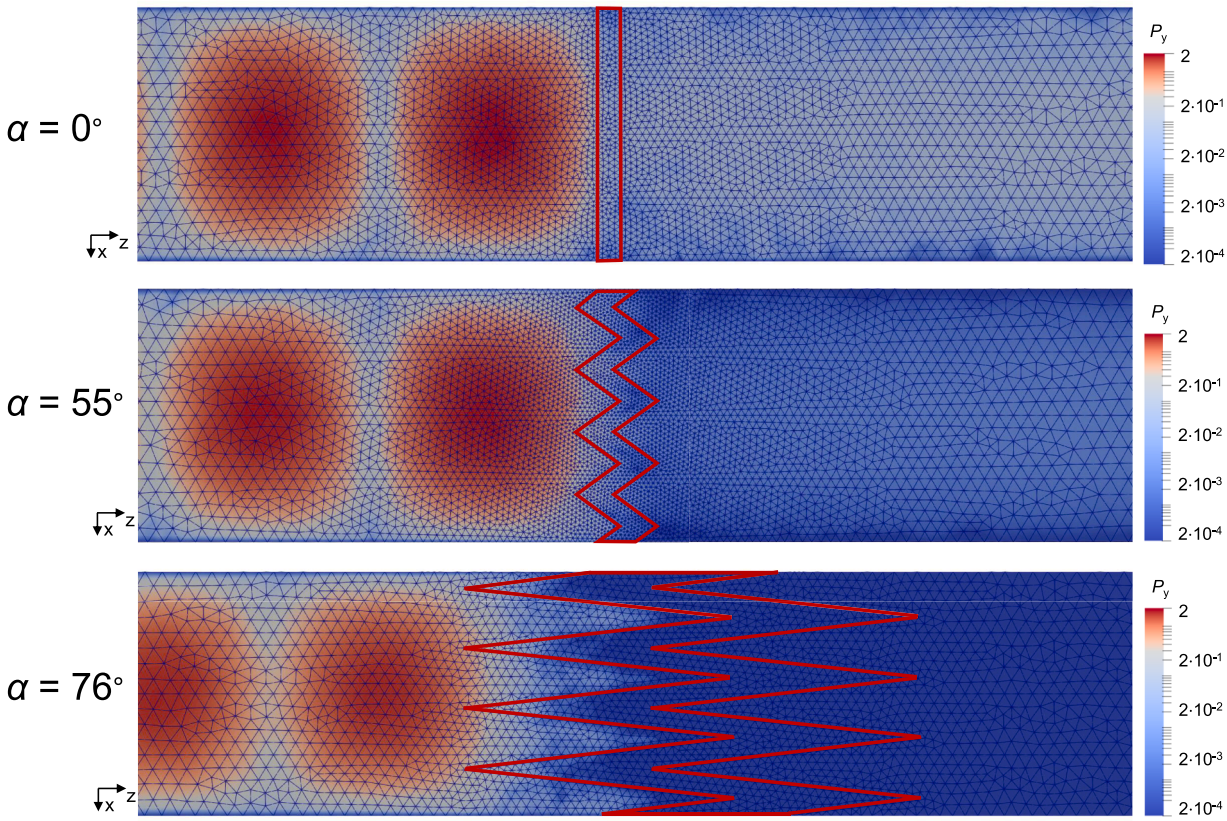

Fig. 10. Contour plots of the normalised magnitude of the electric field in the y-direction, P_y, for sawtooth-shaped layers with different values of inclusion angle α and identical values of a/w (= 4), t (= 2 mm), λ_0 (= 30 mm), and ε (= 45 – 60i).

depending on the incident wave's frequency [25]. The reflected waves interact with neighboring peaks of lossy dielectric material and either constructive or destructive interference between the scattered waves from neighboring peaks may take place [51]. Second, the increase in strut alignment with the wave propagation direction increases the travel length, and therefore net travel time, of the waves in the absorbing lossy dielectric shield. This leads to reduced transmission and increased absorbance. Third, the mismatch in permittivity between the air and the shield material results in internal wave reflections. The travel time of these internally-reflected waves within the shield and, possibly, the constructive or destructive interference of these waves are both depending on the value of α [52]. Shen and co-workers also observed a transition from reflection-dominated to absorption-dominated shielding when reducing the obliqueness of the sawtooth struth. In their parametric study they changed the value of a/w when changing the value of α [14]. Our calculations indicate that the ratio of absorbed to reflected power also depends on the number of periodic base units in the waveguide.

It is insightful to cross-plot the calculated response in Figs. 9 on a A/R versus SE_{tot} diagram, see Fig. 11. In general, increasing the inclusion angle increases both the value of the total shielding effectiveness and the A/R ratio. For a flat, homogeneous polymer nanocomposite layer a trade-off typically exists between SE_{tot} and A/R: increasing the value of the permittivity or thickness of the layer gives a higher SE_{tot} value but often decreases the value of A/R, leading to reflection-dominated ($A/R < 1$) shielding. This trade-off is highlighted in the next paragraph when discussing the role of the value of the permittivity on the shielding performance of the sawtooth-shaped layer (and apparent from shielding measurement data on polymer nanocomposite shields in the literature [53,54]). In contrast, when making use of a sawtooth-shaped design, the inclusion angle can be used as a design parameter to increase both the value of SE_{tot} and the value of A/R (while keeping the permittivity and layer thickness constant). The data in Fig. 11 also indicate that the A/R versus SE_{tot} trend converges for a sufficiently large number of repeat units ($a/w \geq 4$). Increasing the number of repeat units per waveguide width corresponds to a decrease in the confining effect of the waveguide walls on the measured shielding response. The converging behaviour of the predicted A/R versus SE_{tot} response for $a/w \geq 4$ indicates that this response may be identical to that of the limit case of an infinitely long sawtooth-shaped layer subjected to a planar wave in free space.

We proceed by exploring the sensitivity of the sawtooth-shaped layer to normalised layer thickness, t/λ_0. The computed values of A/R and SE_{tot} are plotted as a function of t/λ_0 for sawtooth-shaped layers with an identical value of α (= 30°), see Figs. 12a and 12b, respectively. The calculated data shown in Fig. 12 with a solid line were obtained by varying the value of the thickness (0.1 mm < t < 6 mm) for selected values of a/w and $\lambda_0 = 30$ mm. An additional series of calculations for $a/w = 1$ were conducted for $\lambda_0 = 25$ mm ($f_0 =$ 12 GHz) and $\lambda_0 = 37.5$ mm ($f_0 = 8$ GHz), and are highlighted with a dashed line in Fig. 12. Inspection of Fig. 12 reveals that for both the SE_{tot} and the A/R response the curves for different frequencies are close to identical for the explored range of t/λ_0. The predictions indicate that the total shielding effectiveness monotonously increases with increasing value of the normalised layer thickness. In

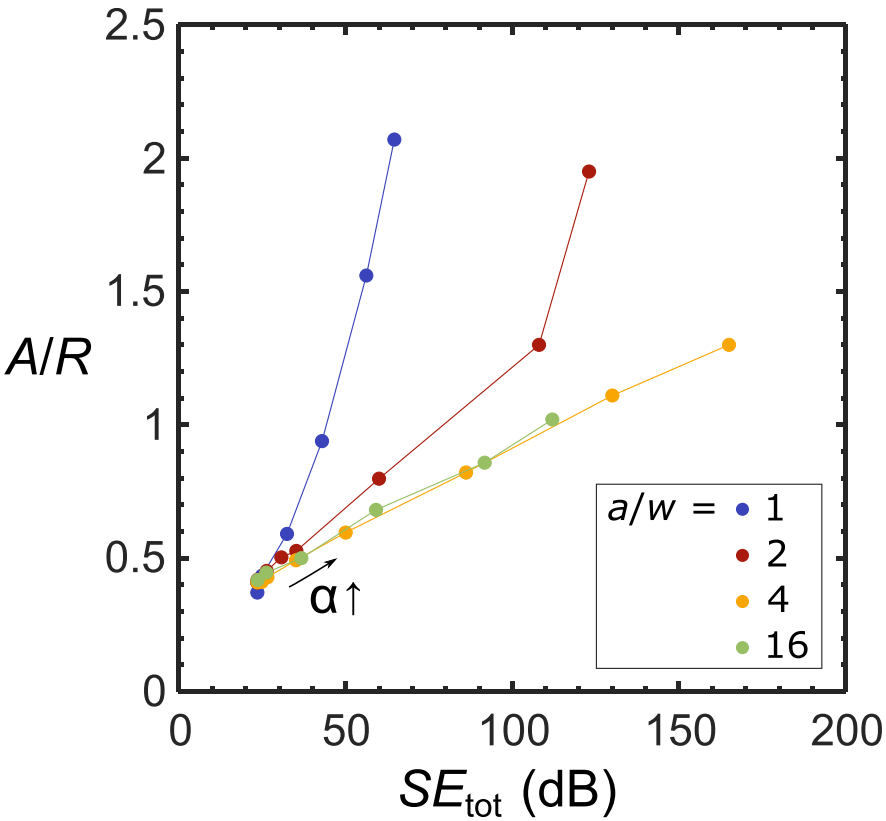

Fig. 11. A/R ratio versus shielding effectiveness with calculated data shown in Fig. 9. Calculations were conducted for $t = 2$ mm, $\lambda_0 = 30$ mm, and $\varepsilon = 45 - 60i$.

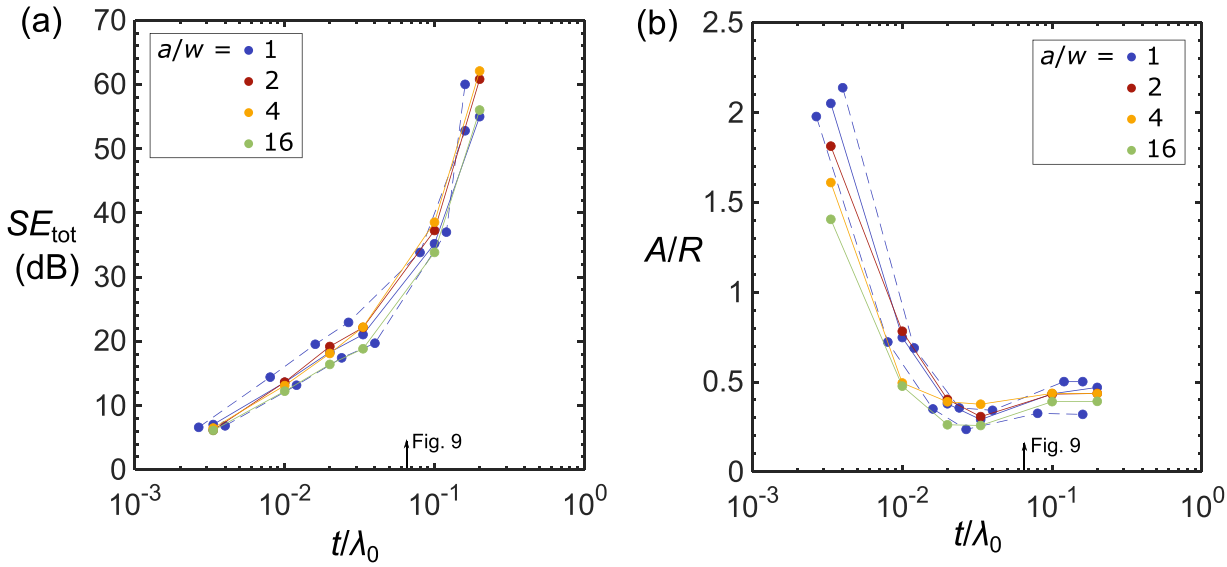

Fig. 12. (a) Total shielding effectiveness SE_{tot} and (b) A/R ratio as a function of normalised thickness t/λ_0 for sawtooth-shaped layers with a/w ranging from 1 to 16 and inclusion angle $\alpha = 30\,^{\circ}$ Calculations were conducted for $\varepsilon = 45 - 60i$ with t in the range 0.1 mm to 6 mm. Solid lines are used for calculations where the nominal wavelength λ_0 is equal to 30 mm ($f_0 = 10$ GHz). Additional calculations for $a/w = 1$ with $\lambda_0 = 25$ mm ($f_0 = 12$ GHz) and $\lambda_0 = 37.5$ mm ($f_0 = 8$ GHz) are included (see dashed lines). An indicator of the t/λ_0 (≈ 0.07) reference value for the predictions shown in Fig. 9 is also included.

contrast, the computed A/R response exhibits a minimum at t/λ_0 close to 0.03. In addition, there is a transition from absorption-dominated shielding ($A/R > 1$) at low values of t/λ_0 to reflection-dominated shielding ($A/R < 1$) at increased t/λ_0 values. This trend, as well as the inverse relation between A/R and SE_{tot} is in line with the typical layer thickness-dependence of flat nano-composites shields.

It remains to illustrate the role of relative permittivity ε on the computed shielding performance of the sawtooth-shaped layer. The complex permittivity of a polymer nanocomposite material with a non-conductive matrix is a function of the nature, shape and concentration of conductive filler material [6,7]. Exploring the entire range of physically relevant values of ε is beyond the scope of the present paper. Here, we adopt a pragmatic approach to illustrate the role of permittivity on the attainable SE_{tot} and A/R space by multiplying the measured reference value of $\varepsilon = 45 - 60i$ with a factor m. The computed shielding response on an A/R - SE_{tot} diagram for a sawtooth layer with inclusion angle in the range of 0° to 80° for selected values of m is shown in Fig. 13. The selected value of the normalised thickness, t/λ_0, is equal to 0.07 and the number of units per waveguide width, a/w, is equal to 4. Different combinations of values of t/λ_0 and a/w give similar insights on the role of ε (data not shown). Consider first the limit case of a flat layer where $\alpha = 0°$, these are highlighted with non-filled markers in Fig. 13. For a relatively low value of permittivity ($m = 0.1$) the response is close to absorption-dominated. Increasing the value of the permittivity by increasing the value of m, increases the total shielding effectiveness, but decreases the value of A/R, this illustrates the typical trade-off between A/R and SE_{tot} for a flat polymer nanocomposite layer. Now, consider the case of a sawtooth-shaped layer where α has a non-zero value. The values of SE_{tot} and A/R increase with increasing value of the inclusion angle in agreement with the curves shown in Fig. 11. The slope of the A/R-SE_{tot} curve is found to be sensitive to the value of m. For values of m close to and above 3 (corresponding to $\varepsilon \geq 135 - 180i$) the shielding response remains reflection-dominated for the entire range of α. For these high permittivity values, the increased wave power reflection due to the increased impedance mismatch at the air-layer interface dominates over the aforementioned wave absorption mechanisms for large inclusion angles.

From a practical point of view, the relation between material volume (and correspondingly mass) in the shield and the shielding performance is of importance for weight-critical applications. Geometric analysis reveals that the total volume of the sawtooth-shaped layer scales linearly with the product of t and $\cos(\alpha)^{-1}$. The predictions in this case study demonstrate that increasing the volume of the layer via the thickness or via the inclusion angle have distinct effects. For a selected value of α, increasing the value of the normalised thickness t/λ_0 (or permittivity ε) decreases the A/R value and increases the value of SE_{tot}, which may result in a transition from absorption- to reflection-dominated shielding. In contrast, increasing the value of the inclusion angle α for a selected combination of t/λ_0 and ε increases both the value of A/R and SE_{tot}. The transition from absorption- to reflection-dominated shielding may be shifted to higher SE_{tot} values via the choice of the inclusion angle. This outcome reveals a possible design strategy which may be exploited to manufacture absorption-dominated polymer nanocomposite shields of sufficiently high shielding effectiveness [14]. Note that the peak-to-peak amplitude of the sawtooth layer scales with the product of w and $\tan(\alpha)$. Depending on the shielding application, there may be a constraint on the local thickness of the shield, and thus the value of α, and therefore a limit in the attainable combination of A/R and SE_{tot} values. The insights on the role of non-dimensional parameters α, t/λ_0 and ε on the A/R versus SE_{tot} shielding behaviour of a sawtooth-shaped polymer nanocomposite layer when tested in a rectangular waveguide are summarised in the sketch shown in Fig. 14.

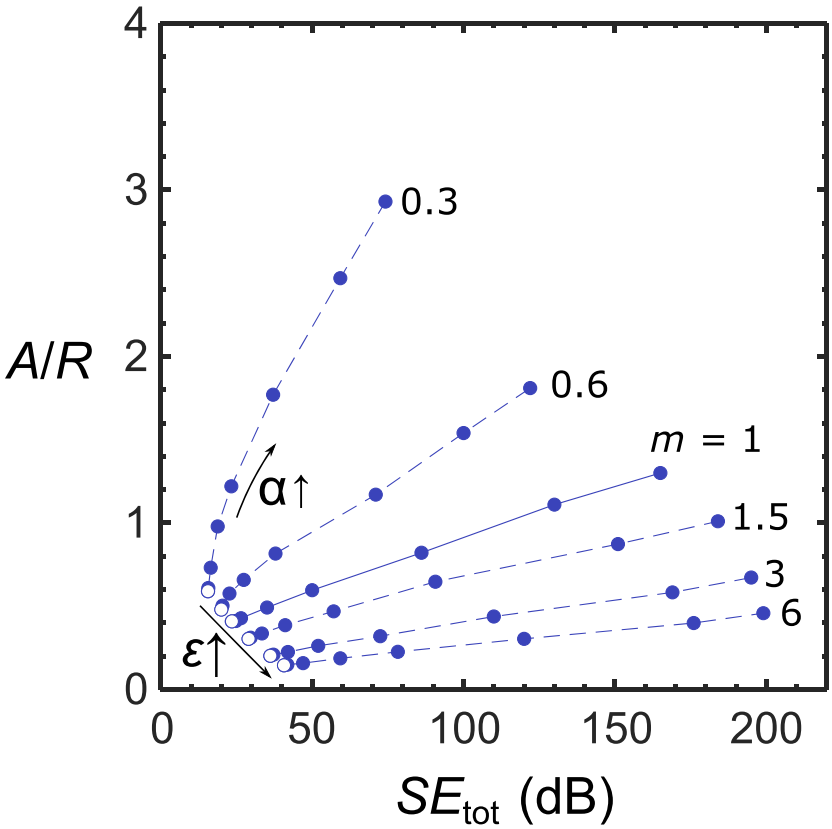

Fig. 13. A/R ratio versus SE_{tot} for a sawtooth-shaped layer of thickness t equal to 2 mm, a/w equal to 4, and inclusion angle ranging from 0° to 80°. Calculations are conducted for $\lambda_0 = 30$ mm and selected permittivity values: $\varepsilon = m \times \varepsilon_{ref}$, where $\varepsilon_{ref} = 45 - 60i$ and the value of m ranges from 0.3 to 6. Data for $\alpha = 0°$ are highlighted with non-filled markers.

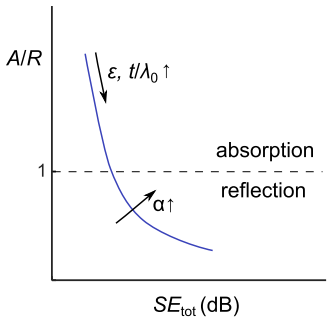

Fig. 14. Sketch of the effect of the non-dimensional parameters α, ε and t/λ_0 on the A/R versus SE_{tot} behaviour of a sawtooth-shaped polymer nanocomposite layer in a rectangular waveguide.

5. Concluding remarks

A three-dimensional numerical model to simulate the electric field distribution within a rectangular waveguide loaded with a polymer nanocomposite shield was developed and used in a case study. Emphasis is placed on the general implementation of the model to accurately predict the EMI shielding performance of a polymer composite sample with freedom in shape and relative permittivity distribution. To this end, the governing set of coupled, real-valued matrix equations is directly solved via a finite element approach. Good agreement is obtained between predictions by the model and those by analytical theory (free space) or commercial software (waveguide) for the limit case of a flat, homogenous layer. To highlight the capability of the model to analyse more complex shield designs, we conducted a numerical case study to explore the role of geometry and relative permittivity of a sawtooth-shaped layer in its shielding performance in a rectangular waveguide. It was found that increasing the inclusion angle, which is proportional to the ratio

of sawtooth amplitude and repeat unit width, increases both the total shielding effectiveness, SE_{tot}, and the ratio of absorbed to reflected wave power, A/R. In contrast, increasing the normalised thickness and/or the permittivity value increases the shielding effectiveness but may result in a transition from absorption-dominated to reflection-dominated shielding.

CRediT authorship contribution statement

F. Van Loock: Conceptualization, Data curation, Formal analysis, Investigation, Methodology, Software, Validation, Visualization, Writing – original draft. **P.D. Anderson:** Resources, Software, Supervision, Writing – review & editing. **R. Cardinaels:** Conceptualization, Funding acquisition, Investigation, Project administration, Resources, Supervision, Writing – review & editing.

Declaration of competing interest

The authors declare that they have no known competing financial interests or personal relationships that could have appeared to influence the work reported in this paper.

Data availability

Data will be made available on request.

Acknowledgements

This project has received funding from the European Research Council (ERC) under the European Union's Horizon 2020 research and innovation programme: Grant Agreement No. 948739 – PEM-SPrint. The authors would like to thank P. Ravichandran (KU Leuven) for assistance with the numerical simulations in ANSYS.

Supplementary materials

Supplementary material associated with this article can be found, in the online version, at doi:10.1016/j.apm.2024.05.029.

Appendix A

Analytical model to calculate the shielding performance of a flat, uniform layer in free space

Consider a straight, uniform layer of thickness t endowed with complex permittivity, ε, see Fig. A1. A uniform plane wave characterised by wavenumber k_0 ($= 2\pi f_0/c_0$) is orthogonally incident to the left side of the layer. The electric field amplitude of the plane wave at the left air-layer interface is the sum of the electric field amplitude of the incident, right-going wave, $E_{1,+}$, and the amplitude of a reflected, left-going wave, $E_{1,-}$. There is no incident wave on the second layer-air interface; the field amplitude of the transmitted, right-going plane wave at this interface reads $E'_{2,+}$. Note that a prime superscript is used for a field amplitude at the right of an interface to distinguish from the field amplitude at the left side. In addition, we make use of '+' and '–' subscripts for field amplitudes of right- and left-going waves, respectively.

Now, the reflectance of the multilayer is defined as:

$$R = \left|\frac{E_{1,-}}{E_{1,+}}\right|^2, \tag{21}$$

and the transmittance reads:

$$T = \left|\frac{E'_{2,+}}{E_{1,+}}\right|^2. \tag{22}$$

We calculate the (complex) values of $E_{1,-}$, $E_{1,+}$ and $E'_{2,+}$ by making use of a standard transfer matrix approach, see, for example, the book of Orfanidis [25]. The field amplitudes at the right side of the first interface are related to the field amplitudes at the left side of the second interface via the following propagation matrix:

$$\begin{bmatrix} E'_{1,+} \\ E'_{1,-} \end{bmatrix} = \begin{bmatrix} e^{ikt} & 0 \\ 0 & e^{-ikt} \end{bmatrix} \begin{bmatrix} E_{2,+} \\ E_{2,-} \end{bmatrix} \tag{23}$$

where $k\ (=\sqrt{\varepsilon}k_0)$ is the complex wavenumber within the layer material. Continuity of the total electric fields at the interface requires the following matching matrix for the field amplitudes at the left and right side of an interface to hold:

$$\begin{bmatrix} E_{i,+} \\ E_{i,-} \end{bmatrix} = \frac{1}{\tau_i} \begin{bmatrix} 1 & \rho_i \\ \rho_i & 1 \end{bmatrix} \begin{bmatrix} E'_{i,+} \\ E'_{i,-} \end{bmatrix} \text{ for } i = 1, 2. \tag{24}$$

where the reflection coefficient, ρ_1, at the first interface reads:

$$\rho_1 = \frac{\eta - \eta_0}{\eta + \eta_0}, \tag{25}$$

and the reflection coefficient, ρ_2, at the second interface reads:

$$\rho_2 = \frac{\eta_0 - \eta}{\eta + \eta_0}, \tag{26}$$

where η_0 is the characteristic impedance of vacuum η_0 (= 377 Ω) and η = ($\eta_0 \varepsilon^{-1/2}$) the complex impedance of the layer. In Eq. (24), τ_i is the transmission coefficient at the left side of interface i:

$$\tau_i = 1 + \rho_i \text{ for } i = 1, 2. \tag{27}$$

Recall $E'_{2,-} = 0$. Combining propagation matrix (Eq. (23)) and the matching matrices (Eq. (24)) at the two interfaces gives the following expressions for the reflectance:

$$R = \left| \frac{\rho_1 + \rho_2 e^{-2ikt}}{1 + \rho_1 \rho_2 e^{-2ikt}} \right|^2, \tag{28}$$

and the transmittance:

$$T = \left| \frac{\tau_1 \tau_2 e^{-ikt}}{1 + \rho_1 \rho_2 e^{-2ikt}} \right|^2 \tag{29}$$

by making use of Eqs. (21) and (22), respectively. The absorbance A is calculated via Eq. (14).

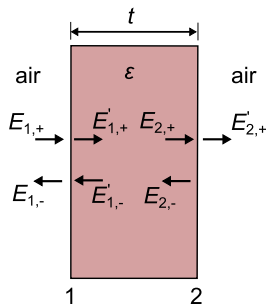

Fig. A1. Field amplitude definitions for the free space analytical model for a lossy dielectric layer.

References

[1] S. Sankaran, K. Deshmukh, M.B. Ahamed, S.K. Khadheer Pasha, Recent advances in electromagnetic interference shielding properties of metal and carbon filler reinforced flexible polymer composites: a review, Compos. Part A Appl. Sci. Manuf. 114 (2018) 49–71, https://doi.org/10.1016/j.compositesa.2018.08.006.

[2] Kok-Swang Tan, Irwin Hinberg, Electromagnetic interference with medical devices. Vitro Laboratory Studies and Electromagnetic Compatibility Standards, Clinical Engineering Handbook, 2004, https://doi.org/10.1016/B978-012226570-9/50068-5.

[3] S. Satyamurthy, S. Savithri, R. Nirmala, A. Devarpiran, A. Ravichandran, A case history of EMI problems of an optoelectronic stabilized sight, in: International Proceedings of the Conference on Electromagnetic Interference and Compatibility, 1997.

[4] S. Geetha, K.K.S. Kumar, C.R.K. Rao, M. Vijayan, D.C. Trivedi, EMI shielding: methods and materials - a review, J. Appl. Polym. Sci. 112 (2009) 2073–2086, https://doi.org/10.1002/app.29812.

[5] D. Wanasinghe, F. Aslani, A review on recent advancement of electromagnetic interference shielding novel metallic materials and processes, Compos. B Eng. 176 (2019), https://doi.org/10.1016/j.compositesb.2019.107207.

[6] J.M. Thomassin, C. Jérôme, T. Pardoen, C. Bailly, I. Huynen, C. Detrembleur, Polymer/carbon based composites as electromagnetic interference (EMI) shielding materials, Mater. Sci. Eng. R: Rep. 74 (2013) 211–232, https://doi.org/10.1016/j.mser.2013.06.001.

[7] F. Qin, C. Brosseau, A review and analysis of microwave absorption in polymer composites filled with carbonaceous particles, J. Appl. Phys. 111 (2012), https://doi.org/10.1063/1.3688435.

[8] L. Ma, M. Hamidinejad, L. Wei, B. Zhao, C.B. Park, Absorption-dominant EMI shielding polymer composite foams: microstructure and geometry optimization, Mater. Today Phys. 30 (2023), https://doi.org/10.1016/j.mtphys.2022.100940.

[9] P. Dubey, M. Gupta, S.I. Kundalwal, Conductive polymer nanocomposite incorporated with carbon nanotubes for effective electromagnetic interference shielding: a numerical study, Polym. Compos. 45 (2024) 3576–3590, https://doi.org/10.1002/pc.28011.

[10] S.C. Tjong, Structural and mechanical properties of polymer nanocomposites, Mater. Sci. Eng.: R: Rep. 53 (2006) 73–197, https://doi.org/10.1016/J.MSER.2006.06.001.

[11] J. Wang, X. Jin, C. Li, W. Wang, H. Wu, S. Guo, Graphene and graphene derivatives toughening polymers: toward high toughness and strength, Chem. Eng. J. 370 (2019) 831–854, https://doi.org/10.1016/J.CEJ.2019.03.229.
[12] C. Huang, X. Qian, R. Yang, Thermal conductivity of polymers and polymer nanocomposites, Mater. Sci. Eng.: R: Rep. 132 (2018) 1–22, https://doi.org/10.1016/J.MSER.2018.06.002.
[13] J. Kruželák, A. Kvasničáková, K. Hložeková, I. Hudec, Progress in polymers and polymer composites used as efficient materials for EMI shielding, Nanoscale Adv. 3 (2021) 123–172, https://doi.org/10.1039/d0na00760a.
[14] B. Shen, Y. Li, D. Yi, W. Zhai, X. Wei, W. Zheng, Strong flexible polymer/graphene composite films with 3D saw-tooth folding for enhanced and tunable electromagnetic shielding, Carbon N Y 113 (2017) 55–62, https://doi.org/10.1016/j.carbon.2016.11.034.
[15] A. Jalali, R. Zhang, R. Rahmati, M. Nofar, M. Sain, C.B. Park, Recent progress and perspective in additive manufacturing of EMI shielding functional polymer nanocomposites, Nano Res. 16 (2023) 1–17, https://doi.org/10.1007/s12274-022-5053-4.
[16] D. Jiang, V. Murugadoss, Y. Wang, J. Lin, T. Ding, Z. Wang, Q. Shao, C. Wang, H. Liu, N. Lu, R. Wei, A. Subramania, Z. Guo, Electromagnetic interference shielding polymers and nanocomposites - a review, Polymer Rev. 59 (2019) 280–337, https://doi.org/10.1080/15583724.2018.1546737.
[17] M. Kamkar, A. Ghaffarkhah, E. Hosseini, M. Amini, S. Ghaderi, M. Arjmand, Multilayer polymeric nanocomposites for electromagnetic interference shielding: fabrication, mechanisms, and prospects, N. J. Chem. 45 (2021) 21488–21507, https://doi.org/10.1039/d1nj04626h.
[18] L.Q. Zhang, B. Yang, J. Teng, J. Lei, D.X. Yan, G.J. Zhong, Z.M. Li, Tunable electromagnetic interference shielding effectiveness via multilayer assembly of regenerated cellulose as a supporting substrate and carbon nanotubes/polymer as a functional layer, J. Mater. Chem. C Mater. 5 (2017) 3130–3138, https://doi.org/10.1039/c6tc05516h.
[19] Q.M. He, J.R. Tao, D. Yang, Y. Yang, M. Wang, Surface wrinkles enhancing electromagnetic interference shielding of copper coated polydimethylsiloxane: a simulation and experimental study, Chem. Eng. J. 454 (2023), https://doi.org/10.1016/j.cej.2022.140162.
[20] L. Omana, A. Chandran, R.E. John, R. Wilson, K.C. George, N.V. Unnikrishnan, S.S. Varghese, G. George, S.M. Simon, I. Paul, Recent advances in polymer nanocomposites for electromagnetic interference shielding: a review, ACS Omega 7 (2022) 25921–25947, https://doi.org/10.1021/acsomega.2c02504.
[21] A. Rajan, S.K. Solaman, S. Ganesanpotti, Design and fabrication of layered electromagnetic interference shielding materials: a cost-effective strategy for performance prediction and efficiency tuning, ACS Appl. Mater. Interfaces 15 (2023) 5822–5835, https://doi.org/10.1021/acsami.2c19016.
[22] A.K. Singh, A. Shishkin, T. Koppel, N. Gupta, A review of porous lightweight composite materials for electromagnetic interference shielding, Compos. B Eng. 149 (2018) 188–197, https://doi.org/10.1016/j.compositesb.2018.05.027.
[23] K. Sushmita, S. Maiti, S. Bose, Multi-layered composites using polyurethane-based foams and 3D-printed structures to curb electromagnetic pollution, Mater. Adv. 3 (2022) 4578–4599, https://doi.org/10.1039/d1ma01089a.
[24] P. Yeh, Optical Waves in Layerd Media, John Wiley & Sons, 1988.
[25] S. Orfanidis, Electromagnetic waves and antennas, 2016.
[26] C. Fang, X. Chen, J. Zhang, X. Xia, G.J. Weng, Study of electromagnetic interference shielding effectiveness of multilayer graphene films by Monte Carlo method, J. Phys. D Appl. Phys. 56 (2023), https://doi.org/10.1088/1361-6463/aca8b4.
[27] Y.-J. Gong, A.D. Klemm, Calculations on nonlinear dielectric slab waveguides by the iterative eigenfimction expansion method, n.d.
[28] J. Jin, The Finite Element Method in Electromagnetics, 3rd ed., Wiley-IEEE Press, 2014.
[29] T. Rybicki, Z. Stempien, I. Karbownik, Emi shielding and absorption of electroconductive textiles with pani and ppy conductive polymers and numerical model approach, Energies (Basel) 14 (2021), https://doi.org/10.3390/en14227746.
[30] S. Matle, S. Sundar, Computation of transmission coefficients in the plain and corrugated electro-magnetic waveguides using finite point set method, Appl. Math. Model. 38 (2014) 1838–1845, https://doi.org/10.1016/j.apm.2013.09.020.
[31] K. Ise, K. Inoue, M. Koshiba, Three-dimensional finite-element solution of dielectric scattering obstacles in a rectangular waveguide, IEEE Trans. Microw. Theory Tech 38 (1990).
[32] R.L. Ferrari, G.L. Maile, Three-dimensional finite-element method for solving electromagnetic problems, Electron. Lett. 14 (1978) 467–468.
[33] J. Córcoles, A. Morán-López, J.A. Ruiz-Cruz, Nested 2D finite-element function-spaces formulation for the mode-matching problem of arbitrary cross-section waveguide devices, Appl. Math. Model. 60 (2018) 286–299, https://doi.org/10.1016/j.apm.2018.03.019.
[34] T.P. Horikis, Dielectric waveguides of arbitrary cross sectional shape, Appl. Math. Model. 37 (2013) 5080–5091, https://doi.org/10.1016/j.apm.2012.10.025.
[35] P. Karimi, M. Ostoja-Starzewski, I. Jasiuk, Experimental and computational study of shielding effectiveness of polycarbonate carbon nanocomposites, J. Appl. Phys. 120 (2016), https://doi.org/10.1063/1.4964691.
[36] Y. Wei, C. Hu, Z. Dai, Y. Zhang, W. Zhang, X. Lin, Highly anisotropic MXene@Wood composites for tunable electromagnetic interference shielding, Compos. Part A Appl. Sci. Manuf. 168 (2023), https://doi.org/10.1016/j.compositesa.2023.107476.
[37] E.G.R. dos Anjos, T.R. Brazil, J. Marini, M.R. Baldan, M.C. Rezende, U. Sundararaj, F.R. Passador, L.A. Pessan, Insights for improving the electromagnetic properties of conductive nanocomposites manufactured with carbon nanotubes, Addit. Manuf. 81 (2024) 103990, https://doi.org/10.1016/j.addma.2024.103990.
[38] A.C. Polycarpou, P.A. Tirkas, C.A. Balanis, The finite-element method for modeling circuits and interconnects for electronic packaging, 1997.
[39] Y. Xu, Y. Yang, D.X. Yan, H. Duan, G. Zhao, Y. Liu, Gradient structure design of flexible waterborne polyurethane conductive films for ultraefficient electromagnetic shielding with low reflection characteristic, ACS Appl. Mater. Interfaces 10 (2018) 19143–19152, https://doi.org/10.1021/acsami.8b05129.
[40] A. Sheng, W. Ren, Y. Yang, D.X. Yan, H. Duan, G. Zhao, Y. Liu, Z.M. Li, Multilayer WPU conductive composites with controllable electro-magnetic gradient for absorption-dominated electromagnetic interference shielding, Compos. Part A Appl. Sci. Manuf. 129 (2020), https://doi.org/10.1016/j.compositesa.2019.105692.
[41] M.M.A. Spanjaards, M.A. Hulsen, P.D. Anderson, Transient 3D finite element method for predicting extrudate swell of domains containing sharp edges, J. Nonnewton Fluid Mech. 270 (2019) 79–95, https://doi.org/10.1016/j.jnnfm.2019.07.005.
[42] C. Mitrias, T.R.N. Egelmeers, N.O. Jaensson, M.A. Hulsen, P.D. Anderson, Simulation of bubble growth during the foaming process and mechanics of the solid foam, Rheol. Acta 58 (2019) 131–144, https://doi.org/10.1007/s00397-018-01123-x.
[43] N.O. Jaensson, M.A. Hulsen, P.D. Anderson, Stokes-Cahn-Hilliard formulations and simulations of two-phase flows with suspended rigid particles, Comput. Fluids 111 (2015) 1–17, https://doi.org/10.1016/j.compfluid.2014.12.023.
[44] C. Mitrias, M.A. Hulsen, P.D. Anderson, Fully implicit interface tracking for a viscous drop under simple shear, Comput. Fluids 184 (2019) 91–98, https://doi.org/10.1016/j.compfluid.2019.03.016.
[45] Y. Seong, T.G. Kang, M.A. Hulsen, J.M.J. Den Toonder, P.D. Anderson, Magnetic interaction of Janus magnetic particles suspended in a viscous fluid, Phys. Rev. E 93 (2016), https://doi.org/10.1103/PhysRevE.93.022607.
[46] T.G. Kang, Y. Gao, M.A. Hulsen, J.M.J. den Toonder, P.D. Anderson, Direct simulation of the dynamics of two spherical particles actuated magnetically in a viscous fluid, Comput. Fluids 86 (2013) 569–581, https://doi.org/10.1016/j.compfluid.2013.08.003.
[47] C. Geuzaine, J.F. Remacle, Gmsh: a 3-D finite element mesh generator with built-in pre- and post-processing facilities, Int. J. Numer. Methods Eng. 79 (2009) 1309–1331, https://doi.org/10.1002/nme.2579.
[48] O. Schenk, K. Gärtner, Solving unsymmetric sparse systems of linear equations with PARDISO, Future Generat. Comput. Syst. (2004) 475–487, https://doi.org/10.1016/j.future.2003.07.011.
[49] W.B. Weir, Automatic Measurement of Complex Dielectric Constant and Permeability at Microwave Frequencies, Proc. IEEE 62 (1974) 33–36, https://doi.org/10.1109/PROC.1974.9382.
[50] X. Lu, A. Zhang, O. Dubrunfaut, D. He, L. Pichon, J. Bai, Numerical modeling and experimental characterization of the AC conductivity and dielectric properties of CNT/polymer nanocomposites, Compos. Sci. Technol. 194 (2020), https://doi.org/10.1016/j.compscitech.2020.108150.
[51] D.D. Lim, S. Lee, J.H. Lee, W. Choi, G.X. Gu, Mechanical metamaterials as broadband electromagnetic wave absorbers: investigating relationships between geometrical parameters and electromagnetic response, Mater. Horiz. (2024), https://doi.org/10.1039/d3mh01959d.

[52] H. Sun, Y. Zhang, Y. Wu, Y. Zhao, M. Zhou, L. Liu, S. Tang, G. Ji, Broadband absorption of macro pyramid structure based flame retardant absorbers, J. Mater. Sci. Technol. 128 (2022) 228–238, https://doi.org/10.1016/J.JMST.2022.04.030.
[53] H. Lee, S.H. Ryu, S.J. Kwon, J.R. Choi, S.B. Lee, B. Park, Absorption-Dominant mmWave EMI Shielding Films with Ultralow Reflection using Ferromagnetic Resonance Frequency Tunable M-Type Ferrites, Nanomicro Lett. 15 (2023), https://doi.org/10.1007/s40820-023-01058-w.
[54] S.H. Ryu, Y.K. Han, S.J. Kwon, T. Kim, B.M. Jung, S.B. Lee, B. Park, Absorption-dominant, low reflection EMI shielding materials with integrated metal mesh/TPU/CIP composite, Chem. Eng. J. 428 (2022), https://doi.org/10.1016/j.cej.2021.131167.